Research Article Vol. 29, No. 2 / 18 January 2021 / Optics Express 1666
Optics EXPRESS

Unidirectional emission and nanoparticle detection in a deformed circular square resonator

ZHENG-ZHENG SHEN,[1,2] MIN TANG,[3] YOU-LING CHEN,[1,2,4] AND YONG-ZHEN HUANG[1,2,5]

[1]State Key Laboratory of Integrated Optoelectronics, Institute of Semiconductors, Chinese Academy of Sciences, Beijing 100083, China
[2]Center of Materials Science and Optoelectronics Engineering, University of Chinese Academy of Sciences, Beijing 100049, China
[3]Institute for Integrative Nanosciences Leibniz IFW Dresden, Helmholtzstraße 20, Dresden 01069, Germany
[4]ylchen@semi.ac.cn
[5]yzhuang@semi.ac.cn

Abstract: We propose a novel deformed square resonator which has four asymmetric circular sides. Photons leak out from specific points, depending on the interplay between stable islands and unstable manifolds in phase space. By carefully breaking the mirror reflection symmetry, optical modes with strong chirality approaching 1 and unidirectional emission can be achieved simultaneously. Upon binding of a nanoparticle, the far-field emission pattern of the deformed microcavity changes drastically. Due to the EP point of the degenerate mode pairs in the deformed cavity, chirality-based far-field detection of nanoparticles with ultra-small size can be realized.

1. Introduction

Over the past few years, optical whispering gallery mode (WGM) microcavities have attracted much research attention due to their high quality (Q) factors and small mode volumes. WGM microcavities have found a wide range of applications including cavity quantum electrodynamics [1,2], nonlinear optics [3,4], low threshold lasing [5–8], and nanoparticle sensing [9–11]. Very recently, WGM microcavities have also been used to explore many interesting phenomena, such as symmetry breaking [12–15], nonreciprocal light transmission [16,17] and exceptional points (EP) [18–20]. It has been proved that when a microcavity works near exceptional point, the sensing signal induced by the perturbation of nanoparticles is greatly amplified [18,21,22]. As a result, WGM microcavity near EP provides a perfect platform for nanoparticle sensing with ultimate sensitivity.

However, due to the rotational symmetry in traditional WGM microcavities, light emission is isotropic. To realize anisotropic emission patterns, rotational symmetry should be broken through special cavity designs such as defects [23], surface treatment of particles [24], boundary deformation [25–27], or coupled cavity [28]. Highly directional emission has been achieved through the incorporation of an air hole into a cylindrical microcavity [23]. By placing two Rayleigh scatterers on the perimeter of a microdisk and tuning their sizes and positions, partially directional emission has been realized [24]. However, the notch or perturbations will greatly degrade the Q factors. Even unidirectional laser emission has been reported through boundary deformation of microcavities. Up to now, unidirectional light emission has been realized in microcavities with various shapes including the spiral [29–31], the limaçon [32], the notched ellipse [33], and the shortegg [34].

#412974 https://doi.org/10.1364/OE.412974
Journal © 2021 Received 23 Oct 2020; revised 14 Dec 2020; accepted 15 Dec 2020; published 11 Jan 2021

Optics EXPRESS

In this work, we have proposed a deformed circular square resonator (CSR) with a novel cavity shape. By carefully breaking the mirror reflection symmetry, chiral resonances with chirality as high as 0.98 and unidirectional emission could be achieved. For the first time to our knowledge, we propose chirality-based far-field nanoparticle detection in a single cavity. Due to the EP point of the degenerate mode pairs in the deformed cavity, nanoparticles with size below 10 nm can lead to striking change of the far field emission. This scheme is especially beneficial for the detection of ultra-small nanoparticles, which removes the need for ultrahigh cavity quality factor. Though sensing based on chiral modes have been realized in rolled-up cavity and cavity with external nanotips close to the rim as local scatterers, the sensing mechanism is mainly based on near-field mode distribution in the form of frequency splitting. Compared with near-field detection, chirality-based far-field sensing eliminates the need for high-resolution spectrometers and complex near-field coupling system, thus pushing the nanoparticle sensors toward real applications.

The paper is organized as follows. Section 2 depicts the physical model of the formation of unidirectional emission in the deformed circular square resonator. Ray dynamics of the cavity is analyzed by calculating the Poincaré surface of section (SOS). Through numerical simulation, the radii of the four circular sides are tuned systematically to optimize the far field emission pattern. In Section 3, nanoparticle detection based on the change of far-field pattern is proposed. In Section 4, robustness of the sensing mechanism is discussed. Section 5 provides a brief conclusion.

2. High chirality and unidirectional emission in the deformed CSR

Schematic diagram of the deformed square microcavity is shown in Fig. 1(a). The microresonator contains four circular sides numbered 1–4 with corresponding radii r_i ($i = 1, 2, 3, 4$), and the flat-side length is a. The cavity material is supposed to be SiO_xN_y with refractive index n = 2.08 and surrounded by air. To study the WGMs in detail, the circular square resonators are numerically studied using the commercial software COMSOL MULTIPHYSICS 4.3b based on finite-element-methods. Generally, using the effective refractive index, the actual 3D structure can be simulated using the 2D model. Two-dimensional simulations have been extensively used in such kind of whispering gallery mode microcavity [26,35–37]. The experimental results correspond well to the 2D simulation results [26,35,36]. The perfectly matched layer (PML) is applied to fully absorb the outgoing waves. The eigenfrequency module was applied to solve the resonant frequencies and field distributions of the modes. The smallest mesh sizes of the cavity and the surrounding air are set to be $\lambda/n/20$ and $\lambda/10$ respectively, where λ=1550 nm.

By designing the parameters of r_i, symmetry of the cavity can be totally broken [25]. Figure 1(b) shows the wavelengths and corresponding Q factors of the TE polarized mode pairs for a totally asymmetric circular square resonator with $r_1 = 33$ μm, $r_2 = 20.4$ μm, $r_3 = 18.5$ μm, and $r_4 = 17$ μm. For the TE polarized mode, the electric field is in the cavity plane and the magnetic field is perpendicular to the cavity plane. It can be found that the mode pairs are almost degenerate, with identical Q factors and wavelengths, indicating that the coupling between the clockwise (CW) and counterclockwise (CCW) modes in the cavity is very weak.

Ray dynamics of the cavity is analyzed through calculating the Poincaré surface of section (SOS). The Poincaré SOSs of a traditional circular square resonator in which $r_1 = r_2 = r_3 = r_4$ and our deformed circular square cavity with $r_1 \gg r_2, r_3, r_4$ are illustrated in Figs. 2(a) and 2(b), respectively. χ is the incident angle of the light ray, and S is the arclength coordinate along the boundary in a counterclockwise direction as shown in the inset of Fig. 2(b). Only the upper halves of the SOSs are presented, because the lower halves have the same patterns. To calculate the Poincaré SOS, 200 light rays with random initial conditions in the phase space are used and the first 500 reflections are recorded for each ray. The islands are embedded in the chaotic sea. As shown in Fig. 2(a), for a traditional CSR, both nondegenerate orbits reflected by adjacent

Optics EXPRESS

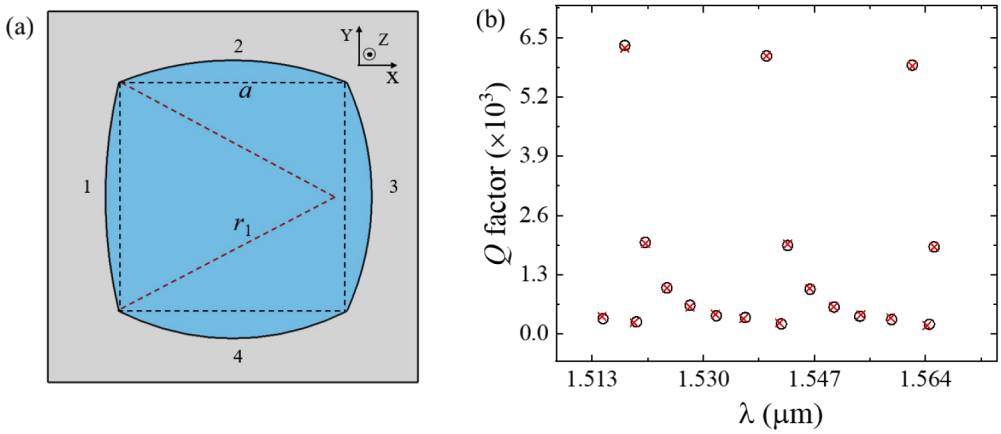

Fig. 1. (a) Schematic diagram of a deformed circular square resonator. The radii of the four circular sides are r_1, r_2, r_3, and r_4. (b) Wavelengths and Q factors of the TE polarized mode pairs. Open circles and crosses mark a pair of coupled modes. The corresponding parameters used in the simulation are: $r_1 = 33$ μm, $r_2 = 20.4$ μm, $r_3 = 18.5$ μm, r_4=17μm, $a = 15.4$ μm.

sides (top islands) and double-degenerate orbits reflected by the opposite sides (bottom islands) can be found. The Poincaré SOS changes dramatically for an asymmetric deformed circular square resonator with $r_1 \gg r_2, r_3, r_4$, as shown in Fig. 2(b). In an asymmetric CSR, positions of the orbits reflected by adjacent edges move significantly. Explicitly, the island at r_1 moves to a lower position of the phase space while the island at its opposite edge r_3 rises to the top. By designing the cavity parameters such as the four radii, cavity modes can be engineered. As a result, it is possible to generate modes with high chirality by optimizing the cavity structure.

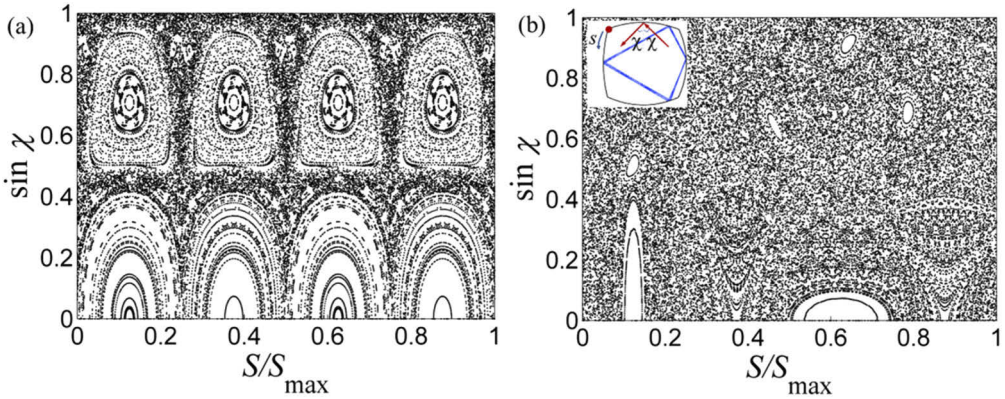

Fig. 2. Poincaré SOS of (a) traditional circular square resonator in which the values of four radii are equal with $a = 15.4$ μm and $r = 20$ μm; (b) deformed square resonator with different radii. The islands represent stable trajectories of the boundary. χ is the incident angle of the light ray, and S represents the arclength coordinate along the boundary in a counterclockwise direction as shown in the inset with the red dot being the start point. The structure parameters are the same as Fig. 1.

To explore the influence of cavity structure in detail, the four radii r_1, r_2, r_3, r_4 are tuned systematically. The cavity wave function can be extended in the orthogonal cylindrical harmonics

Optics EXPRESS

$f_m(\rho)$ as

$$\psi(\rho, \phi) = \sum_{m=-\infty}^{\infty} \alpha_m f_m(\rho) \exp(-im\phi), \tag{1}$$

where (ρ, ϕ) is the polar coordinate, m is the mode number, α_m denotes the corresponding coefficient, and $\exp(-im\phi)$ is the phase factor. The positive (negative) value of m represents the component of the CCW (CW) mode. The wave function $\psi(\rho, \phi)$ can be obtained through COMSOL simulation. As a result, the value of $|\alpha_m|^2$ could be obtained by the integration

$$\int |\psi(\rho, \phi) \exp(im\phi)|^2 \rho d\rho = \int |\alpha_m|^2 |f_m(\rho)|^2 \rho d\rho = |\alpha_m|^2. \tag{2}$$

The chirality is defined as [25]:

$$\alpha = \frac{\sum_{m=-\infty}^{-1} |\alpha_m|^2 - \sum_{m=1}^{\infty} |\alpha_m|^2}{\sum_{m=-\infty}^{-1} |\alpha_m|^2 + \sum_{m=1}^{\infty} |\alpha_m|^2} \tag{3}$$

The value $\alpha = 0$ for a microcavity with rotational symmetry, which means the weights of CW and CCW modes are equal. For example, the standing wave mode in a microring cavity is a superposition of equally weighted CW and CCW modes. For an asymmetric cavity which supports only the CW mode, $\alpha = 1$. The chirality is calculated according to Eq. (3). As shown in Fig. 3(a), under fixed parameters of $r_1 = 33$ μm and $r_3 = 18.5$ μm, the chirality changes drastically with both r_2 and r_4. It should be noticed that along the diagonal direction where $r_2 + r_4 = 37.4$ m, the value of chirality is significantly higher than other zones. The dependence of chirality on the value of r_4 is shown in the inset of Fig. 3(a), where clear transition from nonchiral state to state with high chirality around 1 can be found. When 14 μm $< r_4 <$ 15.5 μm, the mode chirality remains unchanged around 0.69; when r_4 increases from 15.5 μm to 17 μm, α rises from around 0.69 to 0.98; continue increasing r_4 from 17 μm to 18.7 μm, α drops quickly; when $r_4 >$ 18.7 μm, α changes to minus values, indicating that the dominant mode changes from CW to CCW mode. The highest chirality approaching 1 can be realized when $r_1 = 33$ μm, $r_2 = 20.4$ μm, $r_3 = 18.5$ μm, and $r_4 = 17$ μm. For this specific cavity structure, asymmetric scattering induced by the special cavity boundary leads to the competition between CW and CCW mode, resulting in the formation of mode with high chirality. The dependence of chirality on r_1 and r_3 is also simulated, as depicted in Fig. 3(b).

The corresponding mode fields and far field patterns are depicted in Fig. 4. For a rotational-symmetric CSR, the circular sides have a convergence effect on the light ray, so the reflection positions for the resonant modes mainly concentrate at the midpoints of each side while light scattering at the corner is weak [38,39]. As can be seen in Fig. 4(a), light leaks from the midpoints of the four sides due to rotational symmetry, which leads to isotropic far-field emission. By changing the radii of curvatures for the four sides, symmetry in X and Y directions can be broken. When $r_1 \gg r_2 = r_3 = r_4$, which is the case for Fig. 4(b), CW and CCW modes in the cavity exist at the same time due to the symmetry in Y direction, which exit from the midpoint of the arc edge r_1 in two different directions. Explicitly, the CW and CCW modes emit in the 105° and 255° far-field angle. By further tuning $r_2 \neq r_4$, symmetry in Y direction can also be broken. Under values of $r_2 = 20.4$ μm and $r_4 = 17$ μm, only CW mode survives due to the asymmetric backscattering of light [40]. The directionality can be defined as

$$U = \frac{\int I(\theta) \sin(\theta) d\theta}{\int I(\theta) d\theta}, \tag{4}$$

where $I(\theta)$ is the intensity of the far-field distribution at polar angle . U is calculated to be 0.824, which implies a highly unidirectional emission, as shown in Fig. 4(c). The wave function

Optics EXPRESS

is projected to the phase space [41] and the corresponding Husimi distribution is depicted in Fig. 5(a). Islands are almost invisible in the area of $sin > 0$, indicating that the intensity of the CCW mode component is very low and CW component is dominant in the cavity. There are four islands whose centers are distributed at $\sin\chi = -0.56, -0.67, -0.83, -0.68$. For the microcavity with refractive index around 2, total refraction happens when $|\sin|>0.5$. As a result, only light rays in the first island can leak out from the middle of arc r_1. Light rays in the other three islands are well confined inside the cavity through total refraction, and no light escapes from the other three sides. By expanding the modes inside the cavity in cylindrical harmonics, the weights of the CW and CCW modes with different angular mode numbers are calculated, as shown in Fig. 5(b). The chirality α is calculated to be 0.9729 according to Eq. (3). In the phase space of the Husimi projection, the positive and negative values of $\sin\chi$ correspond to the counterclockwise and clockwise direction of light propagation in the cavity. As shown in Fig. 5(a), Husimi projection contains not only the distribution information inside the cavity but also the chirality information of the mode pattern. As a comparison, the chirality can be calculated using another equation [22]

$$\alpha = 1 - \frac{\sum_{ccw} Husimi}{\sum_{cw} Husimi}, \tag{5}$$

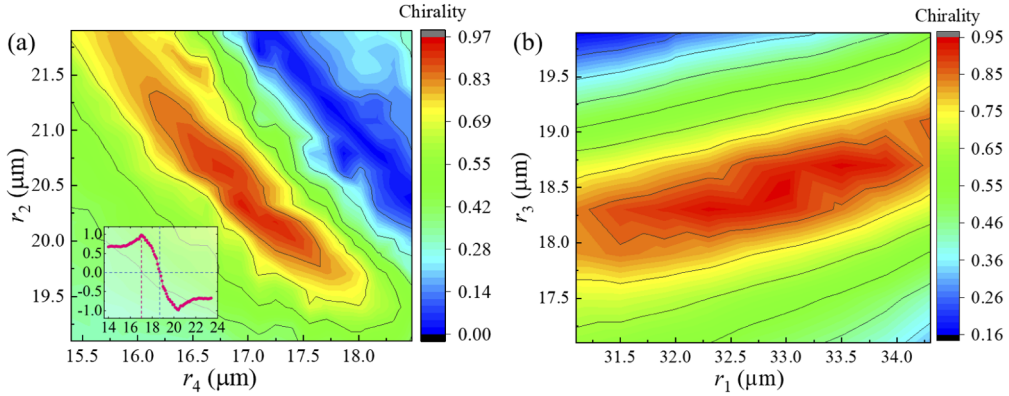

Fig. 3. Dependence of chirality on (a) r_2 and r_4 when keeping $r_1 = 33$ μm and $r_3 = 18.5$ μm. The inset shows chirality versus r_4 when $r_2+r_4 = 37.4$ μm. Transitions from low chirality states to states with strong chirality are observed when $r_4 = 17$ μm/20.4 μm; (b) r_1 and r_3 under fixed $r_2 = 20.4$ μm and $r_4 = 17$ μm.

$\sum_{ccw} Husimi$ denotes the distribution probability of the CCW modes, which can be calculated by making a summation over the distribution probability of the CCW waves from all positions and outgoing directions along the boundary. Similarly, $\sum_{cw} Husimi$ denotes the distribution probability of the CW modes. In Ref. [22], a similar way is used to calculate the chirality of the resonance mode. In our situation, the charity is calculated to be 0.9705. The value of chirality calculated using the two methods agrees with each other. Both the Husimi projection and the angular momentum distribution verify the generation of cavity modes with chirality approaching 1.

Optics EXPRESS

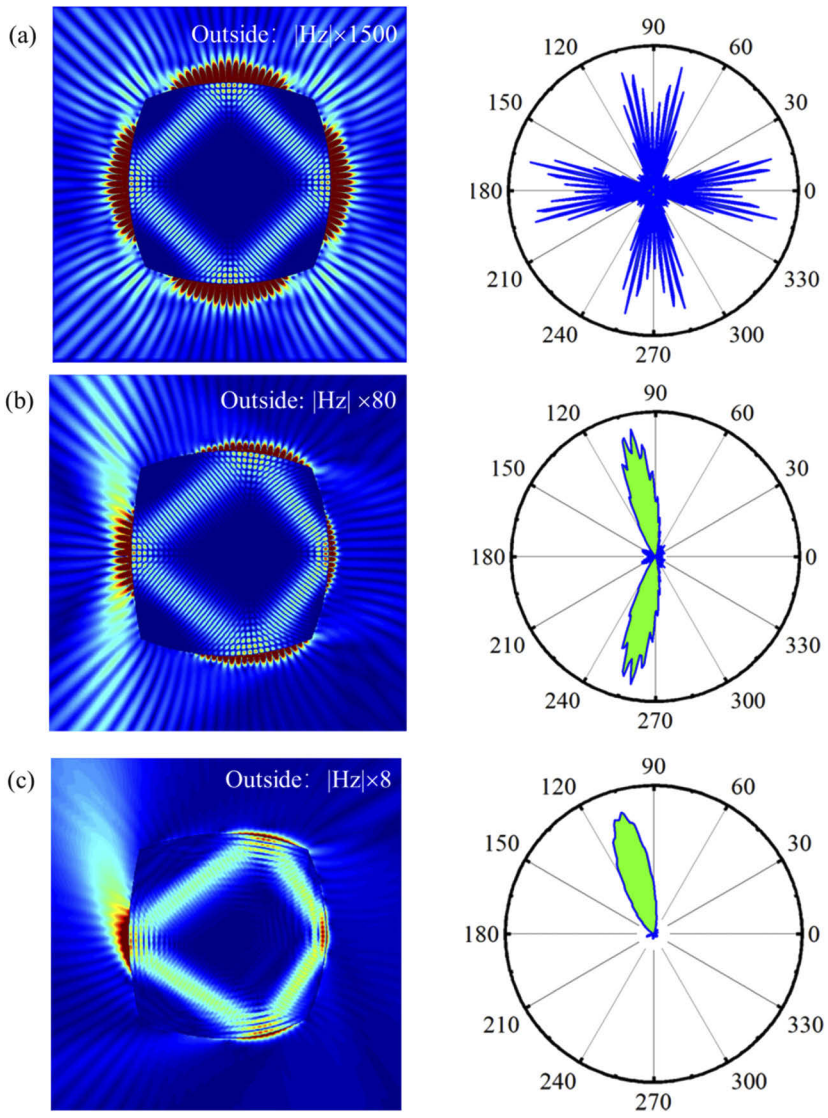

Fig. 4. Magnetic field distribution |Hz| of the fundamental modes for the three cavities with different structures (left panel) and the corresponding far field patterns (right panel). The four radii for the cavities are: (a) $r_1 = r_2 = r_3 = r_4 = 20$ μm (b) $r_1 = 33$ μm , $r_2 = r_3 = r_4 = 20$ μm (c) $r_1 = 33$ μm , $r_2 = 20.4$ μm , $r_3 = 18.5$ μm, $r_4 = 17$ μm . The external mode distribution has been amplified for a better review.

Optics EXPRESS

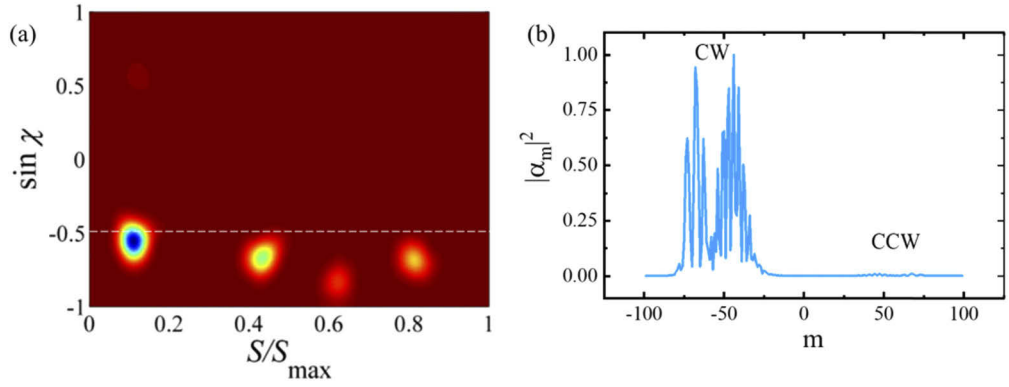

Fig. 5. (a) Husimi projection of the mode in Fig. 4(c). Four islands are distributed in the area of sinχ < 0 which corresponds to the CW component in the cavity, while the CCW mode is almost invisible. The horizontal line represents the criteria for total internal refraction. (b) Coefficient $|\alpha_m|^2$ corresponds to the angular mode number m of the resonance mode in Fig. 4(c). The CCW modes are almost invisible.

3. Nanoparticle detection based on the change of the far-field pattern

Exceptional points (EPs) are singularities which denote the transition from strong coupling to weak coupling. In a non-Hermitian system, when both the eigenvalues and the eigenvectors coalesce for a pair of degenerate modes, EPs are realized. EPs have been reported in many systems including rolled-up cavity [42,43], nanotubes [44] and deformed microdisk [37,45]. When a weak perturbation H_1 <1 interacts with an EP, the induced mode splitting is proportional to $\sqrt{H_1}$. While for a diabolic point, the splitting is proportional to H_1 . As a result, the introduction of EPs promises improvement of the sensitivity of bio/chemical sensing.

By tuning the refractive index n of the cavity material around the wavelength of λ = 1539.4 nm, the real and imaginary part of the wave number for a pair of degenerate modes are recorded. The wave vectors of the degenerate eigenmodes are denoted by $k_\pm = \mathrm{Re}[k_\pm] + \mathrm{iIm}[k_\pm]$. For clarity, $k_\pm$ are shifted by subtracting $(k_+ + k_-)/2$. As shown in Fig. 6(a), when n = 2.08, crossing behavior of the real part and anti-crossing of the imaginary part of the wave vector are observed, indicating that the system is near EP.

The overlap between the pair of modes can be calculated by

$$S = \frac{\left|\int_c dxdy\psi_1^*\psi_2\right|}{\sqrt{\int_c dxdy\psi_1^*\psi_1}\sqrt{\int_c dxdy\psi_2^*\psi_2}}, \tag{6}$$

where Ψ_1 and Ψ_2 represent the wave function for two different modes. After substituting the mode fields into the above equation, the overlap is calculated to be 0.9639, which implies that the two modes are almost identical and nonorthogonal. The mode distribution further corfirms that for the proposed deformed microcavity, the almost degenerate mode pair near EP are no longer orthogonal but almost the same. As shown in Fig. 6(b), the horizontal white dashed line indicates that mode-1 reaches maximum while mode-2 is at secondary maximum. As a comparision, for the standing waves in a traditional symmetric WGM microcavity, symmetry of the cavity requires pairs of orthogonal degenerate modes. When the field distribution of one mode is at maximum, the other is at minimum. These observations further confirm the realization of exceptional point in the deformed cavity.

In the following, we propose to use the unidirectional far-field pattern of the deformed circular square resonator near EP to realize detection of nanoparticles. The cavity parameters are

Optics EXPRESS

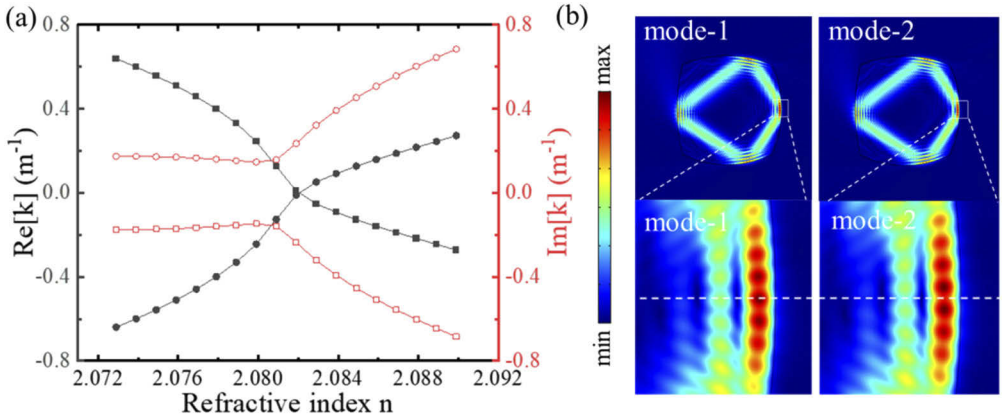

Fig. 6. (a) Real and imaginary parts of the wave vector k versus the refractive index of the deformed circular square resonator. (b) Magnetic field distribution of the degenerate mode pairs in EP states (top panel). The bottom panel is the enlarged view corresponds to the white boxes in the top panel.

fixed as $r_1 = 33$ μm, $r_2 = 20.4$ μm, $r_3 = 18.5$ μm, and $r_4 = 17$ μm. Upon nanoparticle binding, backscattering of light induces coupling between the CW and CCW modes. As a result, the criterion of high chirality generation is broken. The chirality is weakened and the far field distribution changes drastically. Instruments such as CCD cameras enable the probe of far-field distribution, which removes the need for high-resolution spectrometers. The magnetic field distribution along the boundary is calculated, as shown in the top panel of Fig. 7. The position of the nanoparticle is denoted by the angle θ in a clockwise direction as shown in the inset of Fig. 7. When θ = 0, the nanoparticle is attached at the position of vertex A. The four vertexes A, B, C, and D are marked in the figure. The field strength reached maximum near the midpoint of the arc side r_1, while the mode intensity is almost zero at the corners. The dependence of mode chirality

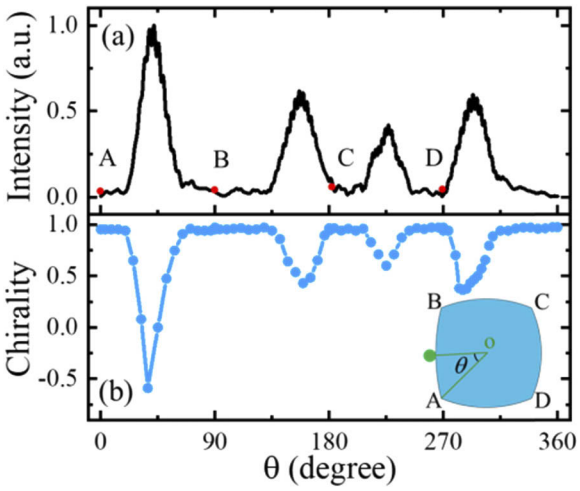

Fig. 7. Numerical simulation of single-nanoparticle detection. (a) Top panel: intensity of the magnetic field along the boundary. (b) Lower panel: dependence of mode chirality on the binding position of the nanoparticle. The inset is the schematic picture of singe-nanoparticle detection on the deformed CSR. Radius of the nanoparticle is fixed at r = 10 nm.

Optics EXPRESS

on the particle binding position is depicted in the lower panel of Fig. 7. The refractive index of the particle is set to be 1.5 to simulate the case for polystyrene and most bioparticles. Radius of the nanoparticle is fixed at $r = 10$ nm. As expected, when the nanoparticle binds to the cavity surface with strong electromagnetic field, the chirality degrades sharply. Furthermore, asymmetric reflection induced by the binding of particles can also lead to reversal of the mode chirality. Explicitly, when a nanoparticle attaches to the hot spot on side r_1 where the field intensity reaches maximum, the chirality changes drastically from around 1 to −0.7. The dominant emission changes from CW to CCW mode in the far field distribution.

The influence of particle size on chirality is simulated when the binding position is set at the hot spot. As depicted in Fig. 8(a), the chirality of the cavity mode decreases rapidly with the increase of particle radius when the particle radius <5 *nm* . When $r = 4$ nm, α is around 0.5. When $r = 5$nm, α rapidly degrades to 0. When 5 nm<r<8 *nm*, the chirality changes to minus values and increases. When $r = 8$ nm, the chirality reaches a value of −0.71. When r is further increased beyond 8 nm, the chirality decreases again. The asymptotic behavior can be explained through the complicated light scattering mechanism of the cavity. There are two main pathways of scatterings. One is the asymmetric scattering originated from the symmetry-broken microcavity, and the other is the scattering induced by the nanoparticle. The two pathways influence each other until reaching a final equilibration.

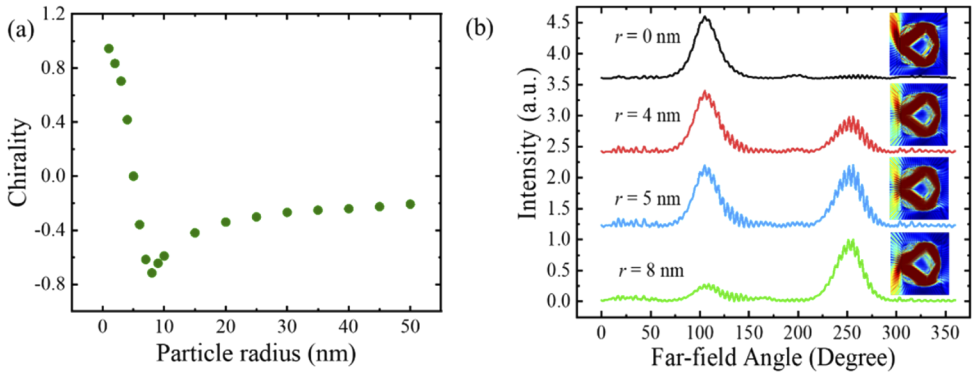

Fig. 8. (a) Mode chirality as a function of the particle radius when the particle binds to the hotspot on the arc side r_1. (b) Far-field mode patterns under different nanoparticle sizes. The lines are vertically shifted for a clear view.

Figure 8(b) shows the far-field intensity under different particle sizes. For a bare deformed circular square resonator, the far field emission is almost unidirectional; when $r = 4$ nm, unidirectional emission changes to two-directional emission, but the weight of CW mode at the emission angle of 105°dominants; when $r = 5$ nm, CW and CCW modes are of almost equal weights; when $r = 8$ nm, the weight of CCW mode at the emission angle of 255°dominates.

4. Discussion

Special attention should be given to the robustness of the sensing scheme.

First, influence of mesh size and surface roughness on the result of COMSOL simulation should be considered. In Section 3, for the region of the nanoparticle, mesh size of 5/6 nm is used. We have done the simulation under a much smaller mesh size of 5/30 nm, and the result is almost the same except for a slight value difference, indicating that the simulation result is robust under mesh sizes which are small enough. Due to the limitation of the etching techniques, surface roughness of the microcavity is inevitable. We have simulated the case of a cavity with

Optics EXPRESS

random roughness of size around 4 nm. The resultant mode distribution is shown in Fig. 9. Almost unidirectional emission is apparent. The corresponding chirality is calculated to be 0.78, which is still sufficient for the realization of nanoparticle sensing.

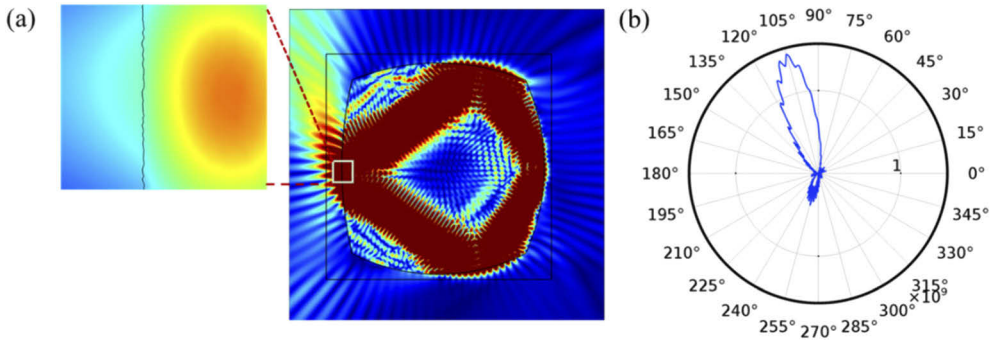

Fig. 9. (a) Magnetic field distribution |Hz| for the deformed microcavity with random surface roughness. The enlarged view shows the roughness added to the boundary. (b) Corresponding far- field distribution under the surface roughness

Moreover, during the experimental realization, the target nanoparticle may bind to positions other than the hot spot. As shown in Fig. 7, as long as the magnetic field intensity of the binding position is nonzero, the chirality as well as the far-field patterns changes compared to the bare cavity, which ensures the realization of nanoparticle detection. Due to the effect of gradient force, targets prefer to attach to the hot spot.

5. Conclusion

We systematically analyzed the mode characteristics of the deformed circular square resonator. The influence of the four curvature radii on the mode chirality, and the corresponding far-field distribution are studied. When the radii of the four sides are equal, the far-field emission pattern is isotropic. Increasing the radius of curvature r_1 while keeping $r_2 = r_3 = r_4$, directional far-field pattern emits from the middle of r_1 . When the size of r_2 and r_4 is further adjusted, unidirectional emission can be obtained at certain cavity structure. When perturbed by a nanoparticle, the far-field pattern of the deformed cavity changes drastically. As a result, the deformed circular square resonator has great potential for bio/chemical sensing. This kind of deformed cavity has many advantages: it supports optical modes with strong chirality approaching 1; the far-field emission divergence angle is narrow; it can work near the exceptional point, thus promising greatly enhanced sensitivity for bio/chemical sensing.

Funding. National Natural Science Foundation of China (11704375, 11974341).

Disclosures. The authors declare no conflicts of interests.

References

1. T. Aoki, B. Dayan, E. Wilcut, W. P. Bowen, A. S. Parkins, T. J. Kippenberg, K. J. Vahala, and H. J. Kimble, "Observation of strong coupling between one atom and a monolithic microresonator," Nature **443**(7112), 671–674 (2006).
2. Y. S. Park, A. K. Cook, and H. Wang, "Cavity QED with diamond nanocrystals and silica microspheres," Nano Lett. **6**(9), 2075–2079 (2006).
3. D. V. Strekalov, C. Marquardt, A. B. Matsko, H. G. L. Schwefel, and G. Leuchs, "Nonlinear and quantum optics with whispering gallery resonators," J. Opt. **18**(12), 123002 (2016).
4. X. F. Jiang, C. L. Zou, L. Wang, Q. Gong, and Y. F. Xiao, "Whispering-gallery microcavities with unidirectional laser emission," Laser Photonics Rev. **10**(1), 40–61 (2016).
5. J. Ward and O. Benson, "WGM microresonators: Sensing, lasing and fundamental optics with microspheres," Laser Photonics Rev. **5**(4), 553–570 (2011).

Optics EXPRESS

6. X. M. Lv, Y. Z. Huang, L. X. Zou, H. Long, and Y. Du, "Optimization of direct modulation rate for circular microlasers by adjusting mode Q factor," Laser Photonics Rev. **7**(5), 818–829 (2013).
7. L. He, Ş. K. Özdemir, and L. Yang, "Whispering gallery microcavity lasers," Laser Photonics Rev. **7**(1), 60–82 (2013).
8. Y. D. Yang, M. Tang, F. L. Wang, Z. X. Xiao, J. L. Xiao, and Y. Z. Huang, "Whispering-gallery mode hexagonal micro-/nanocavity lasers [Invited]," Photonics Res. **7**(5), 594–607 (2019).
9. M. R. Lee and P. M. Fauchet, "Nanoscale microcavity sensor for single particle detection," Opt. Lett. **32**(22), 3284–3286 (2007).
10. F. Vollmer and L. Yang, "Review Label-free detection with high-Q microcavities: a review of biosensing mechanisms for integrated devices," Nanophotonics **1**(3-4), 267–291 (2012).
11. Y. Zhi, X. C. Yu, Q. Gong, L. Yang, and Y. F. Xiao, "Single nanoparticle detection using optical microcavities," Adv. Mater. **29**(12), 1604920 (2017).
12. L. Chang, X. Jiang, S. Hua, C. Yang, J. Wen, L. Jiang, G. Li, G. Wang, and M. Xiao, "Parity-time symmetry and variable optical isolation in active-passive- coupled microresonators," Nat. Photonics **8**(7), 524–529 (2014).
13. B. Peng, S. K. Özdemir, F. Lei, F. Monifi, M. Gianfreda, G. L. Long, S. Fan, F. Nori, C. M. Bender, and L. Yang, "Parity-time-symmetric whispering-gallery microcavities," Nat. Phys. **10**(5), 394–398 (2014).
14. Q. T. Cao, H. Wang, C. H. Dong, H. Jing, R. S. Liu, X. Chen, L. Ge, Q. Gong, and Y.-F. Xiao, "Experimental Demonstration of Spontaneous Chirality in a Nonlinear Microresonator," Phys. Rev. Lett. **118**(3), 033901 (2017).
15. L. Del Bino, J. M. Silver, S. L. Stebbings, and P. Del'Haye, "Symmetry Breaking of Counter-Propagating Light in a Nonlinear Resonator," Sci. Rep. **7**(1), 43142 (2017).
16. J. Kim, M. C. Kuzyk, K. Han, H. Wang, and G. Bahl, "Non-reciprocal Brillouin scattering induced transparency," Nat. Phys. **11**(3), 275–280 (2015).
17. Z. Shen, Y. L. Zhang, Y. Chen, C. L. Zou, Y. F. Xiao, X. B. Zou, F. W. Sun, G. C. Guo, and C. H. Dong, "Experimental realization of optomechanically induced non-reciprocity," Nat. Photonics **10**(10), 657–661 (2016).
18. J. Wiersig, "Enhancing the sensitivity of frequency and energy splitting detection by using exceptional points: Application to microcavity sensors for single-particle detection," Phys. Rev. Lett. **112**(20), 203901 (2014).
19. W. Chen, Ş. K. Özdemir, G. Zhao, J. Wiersig, and L. Yang, "Exceptional points enhance sensing in an optical microcavity," Nature **548**(7666), 192–196 (2017).
20. Y. K. Lu, P. Peng, Q. T. Cao, D. Xu, J. Wiersig, Q. Gong, and Y.-F. Xiao, "Spontaneous T-symmetry breaking and exceptional points in cavity quantum electrodynamics systems," Sci. Bull. **63**(17), 1096–1100 (2018).
21. J. Wiersig, "Sensors operating at exceptional points: general theory," Phys. Rev. A **93**(3), 033809 (2016).
22. N. Zhang, Z. Gu, S. Liu, Y. Wang, S. Wang, Z. Duan, W. Sun, Y.-F. Xiao, S. Xiao, and Q. Song, "Far-field single nanoparticle detection and sizing," Optica **4**(9), 1151–1156 (2017).
23. J. Peter, M. Kailasnath, V. Anand, C. Vallabhan, and A. Mujeeb, "Control of directional emission of resonance modes in an asymmetric cylindrical microcavity," Opt. Laser Technol. **105**, 1–3 (2018).
24. M. Kim, K. Kwon, J. Shim, Y. Jung, and Y. Yu, "Partially directional microdisk laser with two Rayleigh scatters," Opt. Lett. **39**(8), 2423–2426 (2014).
25. J. Wiersig, A. Eberspächer, J. B. Shim, J. W. Ryu, S. Shinohara, M. Hentschel, and H. Schomerus, "Nonorthogonal pairs of copropagating optical modes in deformed microdisk cavities," Phys. Rev. A **84**(2), 023845 (2011).
26. S. Liu, J. Wiersig, W. Sun, Y. Fan, L. Ge, J. Yang, S. Xiao, Q. Song, and H. Cao, "Transporting the Optical Chirality through the Dynamical Barriers in Optical Microcavities," Laser Photonics Rev. **12**(10), 1800027 (2018).
27. J. Wiersig, "Non-Hermitian Effects Due to Asymmetric Backscattering of Light in Whispering-Gallery Microcavities," in *Parity-time Symmetry and Its Applications* (Springer, 2018), pp. 155–184.
28. Y. Z. Hao, F. L. Wang, M. Tang, H. Z. Weng, Y. D. Yang, J. L. Xiao, and Y. Z. Huang, "Widely tunable single-mode lasers based on a hybrid square/rhombus-rectangular microcavity," Photonics Res. **7**(5), 543–548 (2019).
29. M. Kneissl, M. Teepe, N. Miyashita, N. Johnson, G. Chern, and R. Chang, "Current-injection spiral-shaped microcavity disk laser diodes with unidirectional emission," Appl. Phys. Lett. **84**(14), 2485–2487 (2004).
30. M. Hentschel and T.-Y. Kwon, "Designing and understanding directional emission from spiral microlasers," Opt. Lett. **34**(2), 163–165 (2009).
31. M. Hentschel, T. Y. Kwon, M. A. Belkin, R. Audet, and F. Capasso, "Angular emission characteristics of quantum cascade spiral microlasers," Opt. Express **17**(12), 10335–10343 (2009).
32. J. Wiersig and M. Hentschel, "Combining directional light output and ultralow loss in deformed microdisks," Phys. Rev. Lett. **100**(3), 033901 (2008).
33. Q. J. Wang, C. Yan, N. Yu, J. Unterhinninghofen, J. Wiersig, C. Pflügl, L. Diehl, T. Edamura, M. Yamanishi, H. Kan, and F. Capasso, "Whispering-gallery mode resonators for highly unidirectional laser action," Proc. Natl. Acad. Sci. U. S. A. **107**(52), 22407–22412 (2010).
34. M. Schermer, S. Bittner, G. Singh, C. Ulysse, M. Lebental, and J. Wiersig, "Unidirectional light emission from low-index polymer microlasers," Appl. Phys. Lett. **106**(10), 101107 (2015).
35. N. C. Frateschi and A. F. Levi, "The spectrum of microdisk lasers," J. Appl. Phys. **80**(2), 644–653 (1996).
36. H. Z. Weng, Y. D. Yang, J. L. Xiao, Y. Z. Hao, and Y. Z. Huang, "Spectral engineering for circular-side square microlasers," Opt. Express **26**(8), 9409–9414 (2018).
37. C. H. Yi, J. Kullig, and J. Wiersig, "Pair of exceptional points in a microdisk cavity under an extremely weak deformation," Phys. Rev. Lett. **120**(9), 093902 (2018).

Optics EXPRESS

38. H. Z. Weng, Y. Z. Huang, Y. D. Yang, X. W. Ma, J. L. Xiao, and Y. Du, "Mode Q factor and lasing spectrum controls for deformed square resonator microlasers with circular sides," Phys. Rev. A **95**(1), 013833 (2017).
39. M. Tang, Y. D. Yang, H. Z. Weng, J. L. Xiao, and Y. Z. Huang, "Ray dynamics and wave chaos in circular-side polygonal microcavities," Phys. Rev. A **99**(3), 033814 (2019).
40. J. Ryu, J. W. Lee, C. H. Yi, J. H. Kim, I. G. Lee, H. S. Kim, S. B. Kim, K. R. Oh, and C. M. Kim, "Chirality of a resonance in the absence of backscatterings," Opt. Express **25**(4), 3381–3386 (2017).
41. M. Hentschel, H. Schomerus, and R. Schubert, "Husimi functions at dielectric interfaces: Inside-outside duality for optical systems and beyond," EPL **62**(5), 636–642 (2003).
42. Y. Fang, S. Li, and Y. Mei, "Modulation of high quality factors in rolled-up microcavities," Phys. Rev. A **94**(3), 033804 (2016).
43. Y. Fang, S. Li, S. Kiravittaya, and Y. Mei, "Exceptional points in rolled-up tubular microcavities," J. Opt. **19**(9), 095101 (2017).
44. B. Peng, Ş. K. Özdemir, M. Liertzer, W. Chen, J. Kramer, H. Yılmaz, J. Wiersig, S. Rotter, and L. Yang, "Chiral modes and directional lasing at exceptional points," Proc. Natl. Acad. Sci. U. S. A. **113**(25), 6845–6850 (2016).
45. J. Ryu, S. Gwak, J. Kim, H. H. Yu, J. H. Kim, J. W. Lee, C. H. Yi, and C.-M. Kim, "Hybridization of different types of exceptional points," Photonics Res. **7**(12), 1473–1478 (2019).